Microstructure evolution and intermediate phase-induced varying solubility limits and stress reduction behavior in sodium ion batteries particles of Na_xFePO_4 $(0 < x < 1)$

Tao Zhang*, Marc Kamlah

Institute for Applied Materials, Karlsruhe Institute of Technology, 76344 Eggenstein-Leopoldshafen, Germany

Abstract

The cathode material Na_xFePO_4 $(0 < x < 1)$ of sodium-ion batteries displays complex phase segregation processes with the existence of an intermediate phase, and large volume change during charging/discharging. A chemo-mechanical phase-field model is developed to capture the thermodynamics of phase segregation along with the structural change that occurs in Na_xFePO_4. The multiwell potential of Na_xFePO_4 for the full range of concentration is constructed for the first time. This new model not only captures phase segregation into a sodium-poor phase $FePO_4$ and a sodium-rich phase $Na_{2/3}FePO_4$ but also the solid-solution phase Na_xFePO_4 $(2/3 < x < 1)$. The microstructure evolution in the whole processes of sodiation and desodiation is investigated. The stress assisted diffusion induces the striking behavior of the maximum solubility limit going beyond 2/3 even within two-phase coexistence. Further, the formation of an intermediate phase leads to

*Corresponding author. Tel.: +49 721 608 25857; Fax: +49 721 608 22347.
Email address: tao.zhang@kit.edu (Tao Zhang)

varying solubility limits which agrees with recent experimental observation, as well as a stress reduction behavior. Finally, our work suggests that prolate Na_xFePO_4 particles are mechanically more reliable due to nearly stress-free phases. We expect that the intermediate phase-induced stress reduction behavior provides a new concept for improving mechanical stability and thus better battery performance.
Keywords: Sodium-ion batteries, Phase segregation, Microstructure evolution, Stress evolution, Phase field approach

1. Introduction

Sodium-ion batteries (NIBs) are considered as an attractive alternative to lithium-ion batteries (LIBs) due to the wide availability, abundance, low cost of sodium, and comparable energy density [1, 2]. Similarly to LIBs, sodium ions are shuttled between the cathode and anode during charging and discharging in NIBs, with the electrolyte acting as the transportation medium for those ions. Phosphate based cathode materials, due to the thermal stability and higher voltage, become one of the best candidates for the cathode materials of NIBs [1]. Compared to the other phosphate polyanion cathode materials ($NaVPO_4F$, $Na_3V_2(PO_4)_2F_3$, Na_2FePO_4F etc.), olivine $NaFePO_4$ has the highest theoretical specific capacity of $154mAhg^{-1}$ [1]. By means of an ion exchange method, olivine phase $NaFePO_4$ is typically synthesized via electrochemical insertion of sodium ions into chemically or electrochemically delithiated $FePO_4$ [3–11]. Although Olivine $NaFePO_4$ exhibits the same crystal structure as its lithium counterpart [3, 9], olivine $LiFePO_4$, which is a widely used cathode material for LIBs, the phase segregation thermodynam-

ics between them is totally different. Li_xFePO_4 (LiFPO) undergoes a first-order phase transition between a lithium-poor phase $FePO_4$ and a lithium-rich phase $LiFePO_4$ upon lithium (de)intercalation at room temperature [12]. In contrast to a direct transformation between two phases in LiFPO, an intermediate state at $Na_{2/3}FePO_4$ occurs in Na_xFePO_4 (NaFPO) during insertion and extraction [4–8, 10, 11]. Based on ex situ X-ray diffraction (XRD), the phase diagram of NaFPO consists of a two-phase region and a single-phase region at room temperature [5]. For $0 < x < 2/3$, phase segregation of NaFPO into a sodium-poor phase $FePO_4$ and a sodium-rich phase $Na_{2/3}FePO_4$ is found to be favorable. For $2/3 < x < 1$, there is a solid-solution phase Na_xFePO_4 constituting a single-phase region. On the other hand, although the host material is the same, the volume mismatch between $FePO_4$ and $NaFePO_4$ can reach about 17%, and even the volume mismatch between $FePO_4$ and $Na_{2/3}FePO_4$ is nearly 2 times that between $FePO_4$ and $LiFePO_4$ (about 6.8%) [5].

NaFPO, first proposed as a cathode material for NIBs by Moreau et al. [3], has been experimentally studied by several groups [4–8, 10, 11, 13]. Based on ex situ XRD and TEM analysis, Casas-Cabanas et al. [4] reveal that the extraction process occurs in two voltage plateaus separated by an intermediate phase $Na_{2/3}FePO_4$, while three phases ($FePO_4$, $Na_{2/3}FePO_4$, and $NaFePO_4$) can appear simultaneously during dynamic insertion. They attributed this asymmetry to the mechanical aspects of the transformation, due to the larger volume mismatch between $FePO_4$ and $Na_{2/3}FePO_4$ compared to that between $Na_{2/3}FePO_4$ and $NaFePO_4$. Subsequently, Galceran et al. [7] observed varying solubility limits of the sodium content during

the two-phase reaction between $FePO_4$ and $Na_{2/3}FePO_4$, based on in situ XRD experiments. This interesting phenomenon is first observed for a micrometric material. Usually, a dynamic miscibility gap occurs in nanoparticles with dimensions below 100 nm [14–17]. For example, combined neutron and XRD investigation reveals strongly varying solubility limits below particle sizes of 35 nm for LiFPO [14]. However, Galceran et al. [7] also pointed out that resolving such an interesting phenomenon as varying solubility limits in micrometric NaFPO will require additional theoretical work. What is more, they do not disclose how the solubility limits evolve during phase changes. Based on Rietveld refinements of synchrotron operando XRD data, Gaubicher et al. [8] not only displayed the varying solubility limits of NaFPO but also a striking behavior that the solubility limits are extended into the thermodynamically unfavorable region ($2/3 < x < 1$) even within two-phase coexistence. However, the mechanism behind this unexpected and striking phenomenon for NaFPO is still unclear. For phase separating cathode materials, the respective phases possess different lattice constants giving rise to a volume mismatch of, for example, up to about 17% for NaFPO which, in turn, causes mechanical stresses and, thus, leads to particle fracture and capacity loss [18–21]. For thermodynamical reasons, there is a contribution of the stresses to the driving force for diffusion in the host material [22–27]. As far as we know, no experimental reports have revealed how the microstructure of the phase separation, including the interface morphology and solubility limits, as well as the stresses evolve in the whole process of insertion/extraction for NaFPO by now.

From the theoretical side, one aspect that needs to receive attention is

how to model the complex thermodynamics of phase segregation of NaFPO and to elucidate the interaction between microstructure evolution and mechanical stresses. Thermodynamic phase-field modeling is one option to describe diffusion and phase changes in NaFPO. A phase-field model based on the Cahn-Hilliard equation, which is weakly nonlocal [28], relies on a continuous order parameter that is a conserved quantity, thus, leading to diffuse interfaces between adjacent phases with no need for the cumbersome tracking of the position of a sharp interface [29]. A phase-field model for NaFPO is studied for the first time in our work [30] for the spherically symmetric boundary value problem. This work captures the important feature of phase segregation into the sodium-poor phase $FePO_4$ and the sodium-rich phase $Na_{2/3}FePO_4$. Subsequently, we [17] employed this phase-field model [30] to investigate the particle size-dependent miscibility gap behavior of NaFPO and found that the phase segregation is completely suppressed when the particle radius of NaFPO is below 6.4 nm. Recently, the microstructure evolution of NaFPO during insertion has been investigated based on this phase-field model [30], and the dynamics of single wave propagation in spherical particles of NaFPO was obtained [31]. However, the above phase-field model for NaFPO [30] is based on the classical multiwell potential function for a two-phase material [32, 33], which we have formulated such that it is limited to the two-phase region of NaFPO. It means that this model can not take the single-phase region $2/3 < x < 1$ into account. As a result, the above works [17, 30, 31] are just focused on the sodium insertion that belongs to the two-phase region $0 < x < 2/3$, however the whole processes of insertion and extraction, including two-phase region and single-phase region,

can not be represented by such an approach. In order to reach a more precise understanding of NaFPO, it is essential to investigate the evolution of microstructure and stresses in the whole processes of insertion and extraction. Thus, the question arises how to model the complex thermodynamics of phase segregation along with lattice changes, including two-phase region and single-phase region. On the other hand, in contrast to LiFPO, the system of NaFPO goes through an intermediate phase of $Na_{2/3}FePO_4$. What is the role of this intermediate phase? Does it affect the stresses induced in the particles of NaFPO? Furthermore, the electrode consists of particles of a variety of shapes. To our knowledge, no work has investigated the influence of particle geometry on the evolution of microstructure and stresses in NaFPO by now.

In this work, we develop a chemo-mechanical phase-field model for NaFPO that accounts for the complex thermodynamics of phase segregation including two-phase region and single-phase region, lattice changes, and mechanical stresses. We construct the multiwell potential of NaFPO for the full range of concentration for the first time. Our new model not only captures the two-phase segregation between $FePO_4$ and $Na_{2/3}FePO_4$, but also the solid-solution phase Na_xFePO_4 $(2/3 < x < 1)$. We employ this new model to investigate the microstructure evolution of NaFPO during the whole processes of insertion and extraction, by finite element simulations based on the advanced numerical technologies of mesh adaptivity and time step adaptivity, as well as parallelization. Our work not only displays the remarkable behavior of the maximum solubility limit of NaFPO going beyond 2/3 during phase changes but also the mechanism behind this phenomenon. Further-

more, the role of the intermediate phase is studied. The formation of an intermediate phase not only elucidates the phenomenon of varying solubility limits but also leads to a stress reduction behavior. Finally, the influence of particle geometry is investigated. We envision that the intermediate phase-induced stress reduction behavior found for NaFPO holds in general and thus provides a new concept for improving the mechanical stability of phase separating electrode materials.

2. Model development

2.1. Mechanically coupled phase-field model

We propose a mesoscopic mechanically coupled phase-field model for NaFPO, in which the sodium concentration c measured in mol per unit volume is introduced as an order parameter. The system free energy of some domain of volume V is given by

$$\Psi(c, \operatorname{grad} c, \boldsymbol{\varepsilon}) = \int_{\mathcal{B}} \left(\psi^{mwp}(c) + \psi^{gd}(\operatorname{grad} c) + \psi^{cp}(c, \boldsymbol{\varepsilon}) \right) dV. \tag{1}$$

Here, ψ^{mwp} is the multiwell potential that defines the respective phases, which will be constructed for NaFPO later. The gradient energy density

$$\psi^{gd} = k_B T_{ref} N_A c_{max} \left(\frac{1}{2} \lambda |\operatorname{grad} \bar{c}|^2 \right) \tag{2}$$

leads to a diffuse interface between phases with λ being a material constant with units of length squared controlling the thickness of the diffuse interface, and $|\cdot|$ denotes the norm of a vector. Furthermore, $\bar{c}$ is the dimensionless concentration scaled with the maximum sodium concentration c_{max} as $\bar{c} =$

c/c_{max}. k_B, T_{ref}, and N_A are the Boltzmann constant, reference temperature, and Avogadro constant, respectively. The coupling energy density ψ^{cp} which is also called the elastic strain energy density, defining the coupling between diffusion and mechanics, is given by

$$\psi^{cp} = \frac{1}{2}\left(\boldsymbol{\varepsilon} - \frac{1}{3}\Omega\left(c - c_0\right)\mathbf{I}\right) : \mathbb{C} : \left(\boldsymbol{\varepsilon} - \frac{1}{3}\Omega\left(c - c_0\right)\mathbf{I}\right), \tag{3}$$

where $\boldsymbol{\varepsilon}$ is the total strain tensor

$$\varepsilon_{ij} = \frac{1}{2}\left(u_{i,j} + u_{j,i}\right) \tag{4}$$

with u_i being the displacement vector. $\frac{1}{3}\Omega(c-c_0)\mathbf{I}$ is the stress-free volumetric strain induced by sodium insertion or extraction. Ω is the partial molar volume, and c_0 is the initial sodium concentration. The elasticity tensor

$$\mathbb{C} = \frac{E}{2(1+\nu)}\left(\delta_{ik}\delta_{jl} + \delta_{il}\delta_{jk}\right) + \frac{E\nu}{(1-2\nu)(1+\nu)}\delta_{ij}\delta_{kl} \tag{5}$$

is taken to be constant and isotropic with ν being the Poisson number and E being the Young's modulus.

The stress tensor can be derived from the free energy density as [34]

$$\mathbf{T} = \frac{\partial\psi(c, \operatorname{grad} c, \boldsymbol{\varepsilon})}{\partial\boldsymbol{\varepsilon}} = \mathbb{C} : \left(\boldsymbol{\varepsilon} - \frac{1}{3}\Omega\left(c - c_0\right)\mathbf{I}\right). \tag{6}$$

The driving force for diffusion is expressed as the gradient of the chemical potential. Minimizing the system free energy with respect to the concentration gives the chemical potential

$$\mu = \frac{\delta\Psi}{\delta c} = \frac{\partial\psi^{mwp}}{\partial c} - k_B T_{ref} N_A \lambda \operatorname{div}\left(\operatorname{grad}\bar{c}\right) - \Omega\ T_H, \tag{7}$$

where the third term is the coupling chemical potential, and $T_H = 1/3T_{ii}$ is the hydrostatic stress.

The Onsager relation

$$\vec{J} = -\mathbf{M} \cdot \operatorname{grad} \mu \tag{8}$$

defines the mass flux, where the mobility tensor $\mathbf{M}$ is non-negative definite. An isotropic mobility is chosen according to

$$\mathbf{M}(c) = M(c)\,\mathbf{I} = \frac{D_0 c\,(c_{max} - c)}{k_B T_{ref} N_A c_{max}}\mathbf{I}, \tag{9}$$

which is symmetric in the range between zero and maximum concentration and in which D_0 is the diffusion coefficient.

Finally, based on the balances of mass and momentum, respectively, the field equations are given by

$$\frac{\partial c}{\partial t} = \operatorname{div}\left(M(c) \operatorname{grad} \mu\right), \tag{10}$$

$$\operatorname{div} \mathbf{T} = \vec{0}. \tag{11}$$

Equation (10) is the mechanically coupled Cahn-Hilliard diffusion equation, which involves fourth-order spatial derivatives in the concentration and third-order spatial derivatives in the displacement. Equation (11) represents the mechanical equilibrium. Combined with the constitutive equations introduced above, the field equations form a system of partial differential equations for concentration and displacement vector, which need to be solved for given initial and boundary conditions. This is a fourth-order nonlinear initial-boundary-value problem.

2.2. Construction of the multiwell potential and experimental fitting

We now construct the multiwell potential of NaFPO for the full range of concentration. We consider the homogeneous Helmholtz free energy density

in the form

$$\psi^h = k_B T_{ref} N_A c_{max} \left(\bar{\mu}^0 \bar{c} + \frac{T}{T_{ref}} \left(\bar{c} \ln \bar{c} + (1-\bar{c}) \ln (1-\bar{c}) \right) + \bar{c}(1-\bar{c}) \sum_{i=1}^{n} \alpha_i (1-2\bar{c})^{i-1} \right). \quad (12)$$

The first term on the right hand side of Equation (12) is the reference chemical potential [15, 35, 36], and the terms multiplied by absolute temperature T represent the entropy of mixing. The enthalpic effect is given in the form of the Redlich-Kister equation [37]. The coefficients α_i are constants related to the weight of enthalpy and furnish a natural classification of various systems. It should be mentioned that for $n = 1$ the homogeneous Helmholtz free energy density goes back to the form that is suitable for LiFPO. How to determine the above unknown parameters so that the multiwell potential matches the phase segregation thermodynamics of NaFPO? We will address this as follows.

First, the chemical potential μ is related to the open circuit voltage E_{oc} by [38]

$$E_{oc}(\bar{c}, T) = -\frac{1}{eN_A} \mu(\bar{c}, T). \quad (13)$$

The chemical potential μ can be expressed as [39]

$$\mu(\bar{c}, T) = \begin{cases} k_B T N_A \left(\frac{\bar{\psi}^h(\bar{c}_{0+}, T) - \bar{\psi}^h(\bar{c}_{0-}, T)}{\bar{c}_{0+} - \bar{c}_{0-}} \right) & \text{if } \bar{c}_{0-} \le \bar{c} \le \bar{c}_{0+} \\ k_B T N_A \frac{\partial \bar{\psi}^h}{\partial \bar{c}} & \text{for otherwise} \end{cases}, \quad (14)$$

where $\bar{c}_{0-}$ and $\bar{c}_{0+}$ are the so-called binodal concentrations, which can be found by constructing the common tangent to the multiwell potential curve (Maxwell construction). $\bar{\psi}^h$ is the dimensionless form of the homogeneous

Helmholtz free energy density where any terms in the free energy density are normalized according to $\bar{\psi} = \psi/(k_B T_{ref} N_A c_{max})$.

Using Equations (13) and (14), we fit the open-circuit voltage to the experimental data [6] with respect to the unknown parameters, as shown in Fig. 1a. We obtain a good fit with the experimental open-circuit voltage curve with $n = 3, \bar{\mu}^0 = -113.23, \alpha_1 = 1.018, \alpha_2 = 3.501$, and $\alpha_3 = -0.792$. This ensures that the phase segregation occurs at the two binodal concentrations $\bar{c}_{0-} = 0.01$ and $\bar{c}_{0+} = 0.666$ with the Maxwell construction given by

$$\frac{\partial \bar{\psi}^h(\bar{c}_{0-})}{\partial \bar{c}} = \frac{\partial \bar{\psi}^h(\bar{c}_{0+})}{\partial \bar{c}} = \frac{\bar{\psi}^h\left(\bar{c}_{0+}\right) - \bar{\psi}^h\left(\bar{c}_{0-}\right)}{\bar{c}_{0+} - \bar{c}_{0-}}. \tag{15}$$

Due to the influence of $\bar{\mu}^0$, the curve of the homogeneous Helmholtz free energy density looks like a more or less straight line without any visible wells, as shown in Fig. 1b. Because of this, we apply a Legendre transform from the Helmholtz free energy density to the Landau free energy density which is also called the Grand Potential [35, 36]:

$$\bar{\psi}^{mwp} = \bar{\psi}^h(\bar{c}) - \frac{\partial \bar{\psi}^h(0.666)}{\partial \bar{c}}\bar{c} = \bar{\psi}^h(\bar{c}) + 114.25\bar{c}. \tag{16}$$

In the Landau free energy density, the multiwell potential nature of NaFPO becomes obvious that exhibits a doublewell structure with two different relative minima at $\bar{c} = 0.01$ and $\bar{c} = 0.666$, characterizing the sodium-poor phase $FePO_4$ and the sodium-rich phase $Na_{2/3}FePO_4$, respectively, see Fig. 1b. Note that any terms of the free energy density $\bar{\psi}^h$ linear in $\bar{c}$ are irrelevant for the derivation of the diffusion equation with the help of equations (7) and (8). For $2/3 < \bar{c} < 1$, the multiwell potential is of convex shape, representing the solid-solution phase Na_xFePO_4. In the two-phase region

$(0 < \bar{c} < 2/3)$, the Maxwell construction, which connects the neighborhoods of the two minima by a common tangent, gives the volume fractions of the two phases in phase segregated states. The two ranges between the respective tangent points of the Maxwell construction, i.e. the binodal concentrations, and the neighboring inflection points are the "nucleation zones", and phase segregation is initiated upon sufficient disturbance of the system. In the inner zone of concavity between the two points of inflection, which is called the "spinodal decomposition zone", homogeneous sodium concentration states are unstable and phase segregation is initiated in any case. Therefore, this new constructed multiwell potential captures the complex phase segregation thermodynamics of NaFPO that the system goes through an intermediate state at $Na_{2/3}FePO_4$, including the two-phase region and the single-phase region.

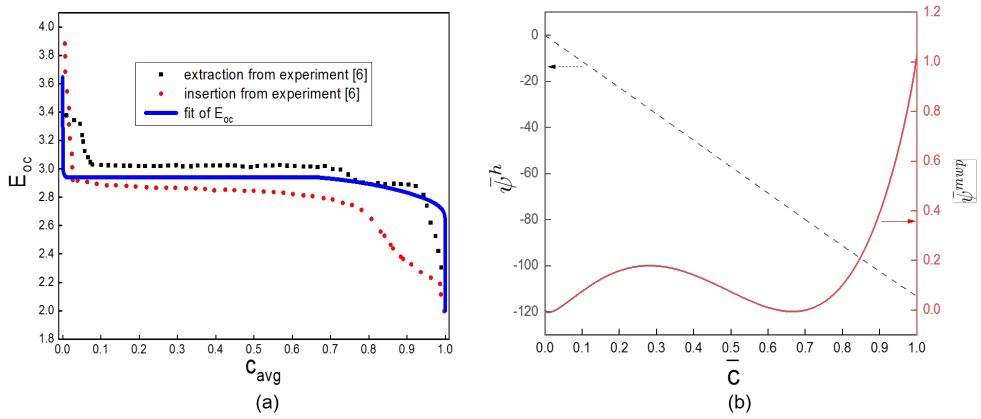

Fig. 1. (a) Fit of the open-circuit voltage to the experimental data [6]. (b) Normalized homogeneous Helmholtz free energy density $\bar{\psi}^h$ and normalized multiwell potential $\bar{\psi}^{mwp}$ as function of $\bar{c}$.

2.3. Boundary conditions

For the purpose of achieving representative statements, we consider in a first step a spherical cathodic particle of radius R_0. Such spherical particle shape is in agreement with the experimental NaFPO sample with a nearly spherical shape in [6, 11]. In a subsequent part of this work, we will investigate the influence of particle geometry. In order to avoid costly expensive 3D simulations, we employ a 2D half particle model using rotational symmetry around the z-axis to replace the 3D problem, as shown in in Fig. 2. Here, cylindrical coordinates are introduced, and all fields are assumed to satisfy

$$c = c(\rho, z, t), \tag{17}$$

$$\vec{u} = u_\rho(\rho, z, t)\vec{e}_\rho + u_z(\rho, z, t)\vec{e}_z. \tag{18}$$

It should be mentioned that the 2D half particle model also can be used to represent ellipsoidal particles with two equal semi-axis.

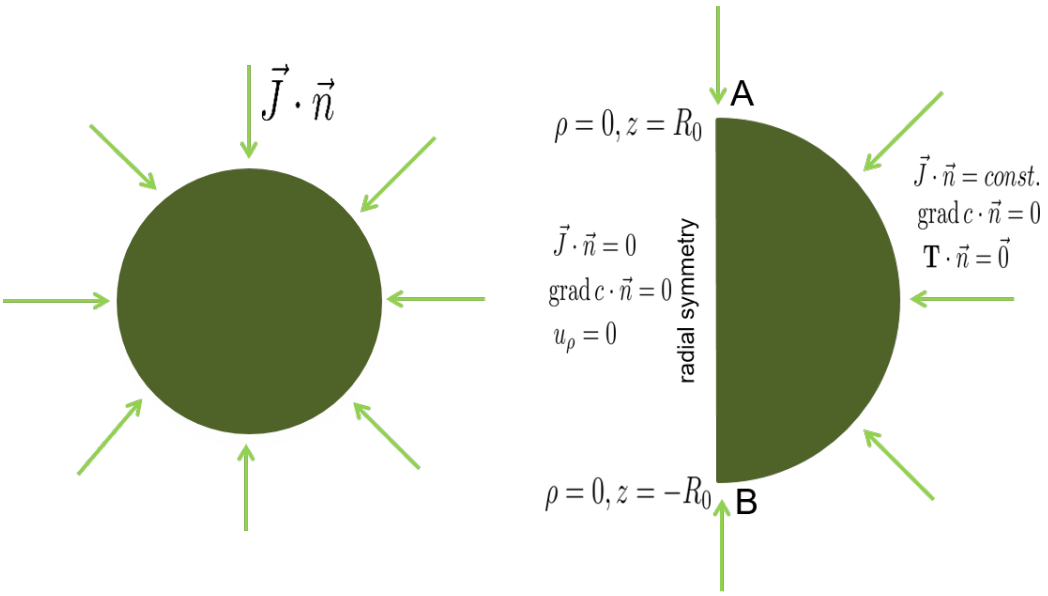

Fig. 2. Boundary conditions for the 2D half particle model.

The boundary conditions are sketched in Fig. 2. We choose a spatially independent mass flux density at the surface as

$$\vec{J}\cdot\vec{n} = \begin{cases} -\frac{C c_{max} V}{3600 \cdot S} & \text{for} \quad c \leq c_{max} \\ 0 & \text{for} \quad c = c_{max} \end{cases}, \tag{19}$$

where $\vec{n}$ refers to the outgoing unit vector normal to the particle surface. Here, V and S are the particle volume and surface, respectively. C is the C-rate, and $C = n$ means that the amount of sodium of a fully charged particle would flow into the particle within $1/n$ hour. Once the maximum concentration c_{max} is reached anywhere at the surface, the mass flux will be stopped.

A vanishing flux condition

$$\vec{J}\cdot\vec{n} = 0 \tag{20}$$

is imposed on the interior boundary AB. In addition, neglecting surface wetting, the "natural" boundary condition [40]

$$\operatorname{grad} c \cdot \vec{n} = 0 \tag{21}$$

is imposed on all boundaries. Equation 21 ensures that the interface between phases is perpendicular to the particle surface [15, 41], when it intersects the surface.

For the mechanical part, the particle is assumed to be stress free at the surface,

$$\mathbf{T} \cdot \vec{n} = \vec{0}, \tag{22}$$

and the interior boundary AB is constrained to have no radial displacement.

2.4. Material parameters

A typical spherical particle radius of $R_0 = 500\ nm$ is chosen. The material parameters for NaFPO are summarized in Table 1, in which the material parameters for LiFPO are also included for comparison. For the detailed determination of the other material parameters for NaFPO, for example, λ, c_{max}, and Ω, see [30]. As mentioned in Introduction section, olivine $NaFePO_4$ is typically synthesized by an ion-exchange method from $LiFePO_4$. According to Yabuuchi et al. [9], lithium ions are chemically or electrochemically extracted from olivine $LiFPO_4$ without destruction of its core structure, forming heterosite-type $FePO_4$. Electrochemical insertion of sodium ions into heterosite-type delithiated $FePO_4$, which possesses the same framework structure with olivine $LiFPO_4$, leading to formation of olivine $NaFPO_4$. As shown in [3, 9], the crystal structures of olivine

$NaFPO_4$ and olivine $LiFPO_4$ are the same. Thus, similar to olivine $LiFPO_4$ [42], olivine $NaFPO_4$ also exhibits a one-dimensional sodium ion diffusion channel, in which sodium ion moves rapidly along the [010] migration channels but has negligible diffusivity in other directions. Actually, not only modeling [43] but also experiment [44, 45] shows that isotropy of the mobility in LiFPO can be enhanced by antisite defects, which are common in battery compounds. We will consider quasistatic insertion/extraction of species into/out of cathodic particles at an extremely low C-rate. Here, $C = 0.001$ is used in the simulations for pherical and oblate particles, and $C = 0.0001$ for prolate particles. In this way, we study the behavior for dynamic, i.e. continuous sodium insertion/extraction very close to a sequence of equilibrium states i.e., the system is allowed to move along a path of relaxed quasi-equilibrium states. Welland et al. [16] have pointed out that the anisotropy of mobility will prefer certain directions of transport, but not influence relaxed system states which are thermodynamically determined. Indeed, Tang et al. [46] also have revealed that the LiFPO cases without and with considering the anisotropy of mobility will eventually exhibit the same equilibrium states that are the most energetically favorable, although the relaxation may be extremely slow for the anisotropic case. Furthermore, Yang and Tang [47] examined the effect of the elastic anisotropy, and reveal that there is a relatively small difference in the phase morphology of LiFPO with and without elastic anisotropy. Hence, it is expected that the anisotropic property has no significant influence on the quasi-equilibrium states of the system that are investigated in our simulations. In order to simplify the current work, we therefore do not take the anisotropy into account in our model. The detailed

discussion of crystal anisotropy, including anisotropic diffusion, anisotropic gradient energy, anisotropic deformation, and anisotropic elasticity, is beyond the scope of this work. One can refer to [15, 36, 46–51] for more information. It should be mentioned that, at room temperature, the miscibility gap of LiFPO encompasses nearly the entire lithium composition range of the material, according to the phase diagram of LiFPO from [12]. However, both in operando X-ray-based measurements [52–54] and modeling studies [15, 50] reveal that the equilibrium phase transition between $FePO_4$ and $LiFePO_4$ could be bypassed by the formation of a metastable solid solution at high (dis)charging rates. Also, a shrinking and eventually disappearing miscibility gap occurs in nanoparticles with dimensions below 100 nm, leading to an obvious solid solution zone in LiFPO [14–17]. Here, as mentioned before, we consider quasistatic insertion of lithium into bulk LiFPO particles with $R_0 = 500\ nm$ at an extremely low C-rate of $C = 0.001$, such that the phase evolution of LiFPO still obeys the phase behavior shown in the phase diagram of LiFPO from [12].

The resulting set of equations has been implemented in the finite-element, multiphysics framework MOOSE [58] for the solution of the fourth-order nonlinear initial-boundary-value problem. MOOSE allows mesh adaptivity and time step adaptivity, as well as parallelization. Using these advanced numerical capabilities, the time-dependent insertion/extraction process in electrode particles including the coupling to mechanics is simulated. In particular, the mesh adaptivity not only takes the cost of the simulation into account meaning that the mesh should be coarsened in regions of weak gradients, but also effectively handles the numerical difficulty that the moving interface

Table 1

The material parameters for the two cathode materials.

Parameter	NaFPO	LiFPO
$\bar{\mu}^0$	-113.23	-
α_1	1.018	4.5 (Ref. [15])
α_2	3.501	-
α_3	-0.792	-
λ	1.8×10^{-17} (m^2) (Ref. [30])	8.8×10^{-18} (m^2) (Ref. [15])
D_0	1×10^{-15} (m^2/s) (Ref. [30])	1×10^{-14} (m^2/s) (Ref. [43])
c_{max}	2.1×10^4 (mol/m^3) (Ref. [30])	2.29×10^4 (mol/m^3) (Ref. [55])
Ω	8.8×10^{-6} (m^3/mol) (Ref. [30])	2.9×10^{-6} (m^3/mol) (Ref. [56])
E	120 (GPa) (Ref. [30])	124.5 (GPa) (Ref. [57])
ν	0.25 (Ref. [57])	0.25 (Ref. [57])

between phases with its strong gradients requires adequate resolution. Simulations are performed on a high-performance Linux computer cluster.

3. Results and Discussion

In the figures, the average concentration c_{avg}, also called "state of charge" (SOC) is $c_{avg} = \int_{\mathcal{B}} \bar{c} dV/V$, and $\bar{\Psi}_{avg} = \int_{\mathcal{B}} \bar{\psi} dV/V$ is the normalized average system free energy, see also Equation (1).

3.1. Microstructure evolution

First, we study the microstructure evolution of NaFPO during the whole processes of insertion and extraction. Fig. 3a shows the system free energy evolution of NaFPO during insertion and extraction by the solid lines, and

the evolution of the microstructure and the corresponding hydrostatic stress is shown in Fig. 4. In Fig. 3a, for comparison purposes, both, the dimensionless multiwell potential versus normalized concentration and the plot of the system free energy evolution for pure diffusion are also entered. Those parts of the plots, where the solid lines coincide with the dimensionless multiwell potential curve correspond to homogeneous states whereas solid lines nearby the path of the Maxwell construction indicate phase segregated states. We find that due to the contribution from the elastic strain energy, the system free energy at the phase-segregated states is larger than that from the pure diffusion case.

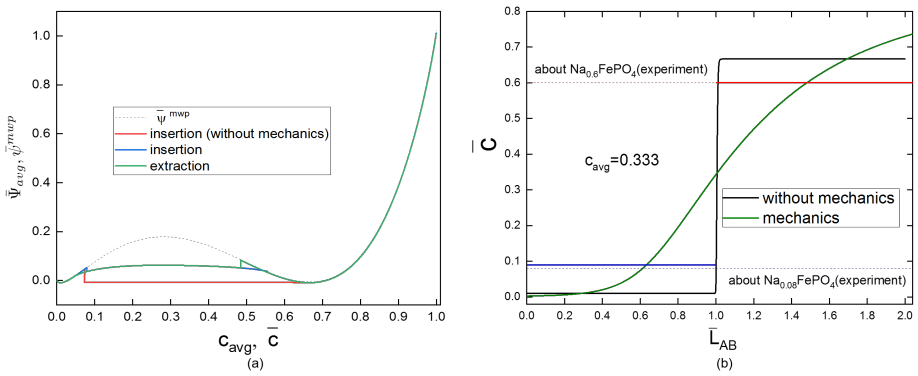

Fig. 3. (a) Normalized average system free energy $\bar{\Psi}_{avg}$ and, for comparison, normalized multiwell potential $\bar{\psi}^{mwp}$ as function of c_{avg} and $\bar{c}$, respectively. (b) Normalized concentration and calculated average solubility limits at $c_{avg} = 0.333$ plotted along the rotational axis AB during insertion. The red straight line represents the calculated high average solubility limit, and the blue straight line represents the calculated low average solubility limit. The dashed horizontal lines represent the experimental results [11].

First, we focus on the insertion process. In Fig. 4a, the system is in

a homogeneous state at the beginning of sodium insertion. Once c_{avg} gets close to 8%, which is a little bit postponed compared to the pure diffusion case, a sodium-rich island is initiated around the "south pole" region, corresponding to the sharp dropping process of the system free energy shown in Fig. 3a. Here, c_{avg} required to initiate a phase separation is consistent with the experimental observation in [8]. The sodium-poor phase $FePO_4$ and the intermediate phase $Na_{2/3}FePO_4$ are recognized. Due to the minimization of the system free energy, NaFPO displays the dynamics of single wave propagation: the single sodium-rich island gradually grows up along the z-direction, and the phase boundary always goes all across the particle. Such single wave propagation behavior is similar to the one experimentally observed in LiFPO [59–62]. In order to minimize the interface, the interface between phases changes from the convex shape to the concave shape with an intermediate shape of plane circularity at $c_{avg} = 33.3\%$. Along the direction of the moving interface, the stresses in each phase shift gradually from tensile stresses to compressive stresses. When c_{avg} grows up to 55.52%, the intermediate phase will occupy all of the particle, which is earlier compared to 66.1% from the pure diffusion case. The later number can be inferred from Fig. 3a, where the red line intersects with the dimensionless multiwell potential. From now on, the system enters the single-phase region, and the solid-solution phase Na_xFePO_4 gradually evolves into $NaFePO_4$. Correspondingly, due to the low C-rate, the single-phase region is at an almost stress-free state.

Strikingly, as can be seen in Fig. 4a for states of average concentration of 33% and 50%, the maximum solubility limit goes beyond 2/3 during

phase changes, which is extended into the thermodynamically unfavorable region. This is in agreement with a recent experimental observation based on Rietveld refinements of synchrotron operando XRD data [8]. What is the mechanism underlying this interesting behavior? The hydrostatic stress contributes to the chemical potential, see Equation (7). Thus the gradient of hydrostatic stress in each phase gives a mechanical contribution to the driving force for diffusion along the z-direction. As a result, as shown in Fig. 3b, in contrast to the constant concentration of 2/3 in each phase from the pure diffusion case, a concentration gradient is evoked in each phase. We see that the concentration inhomogeneity in the high concentration phase leads to this interesting phenomenon that the maximum solubility limit goes beyond 2/3. On the other hand, the average solubility limit is the right quantity for comparison with experimental measurements in which diffraction probes the average species occupancy [14]. Thus, we introduce the average solubility limit to represent the composition in each phase, which is shown as a solid horizontal line in Fig. 3b. Fig. 3b shows the concentration at $c_{avg} = 0.333$ plotted along the rotational axis AB. For comparison purposes, the concentration plot in the absence of mechanics is also entered. The dash horizontal lines in Fig. 3b represent the experimentally measured solubility limits of NaFPO [11]. We find the calculated low and high average solubility limits as $Na_{0.09}FePO_4$ and $Na_{0.6}FePO_4$, respectively. The average miscibility gap between the low and high average solubility limits is reduced compared to the pure diffusion case, which can be explained by the compressing effect of the elastic strain energy. In any case, our calculated average solubility limits are consistent with the experimental values.

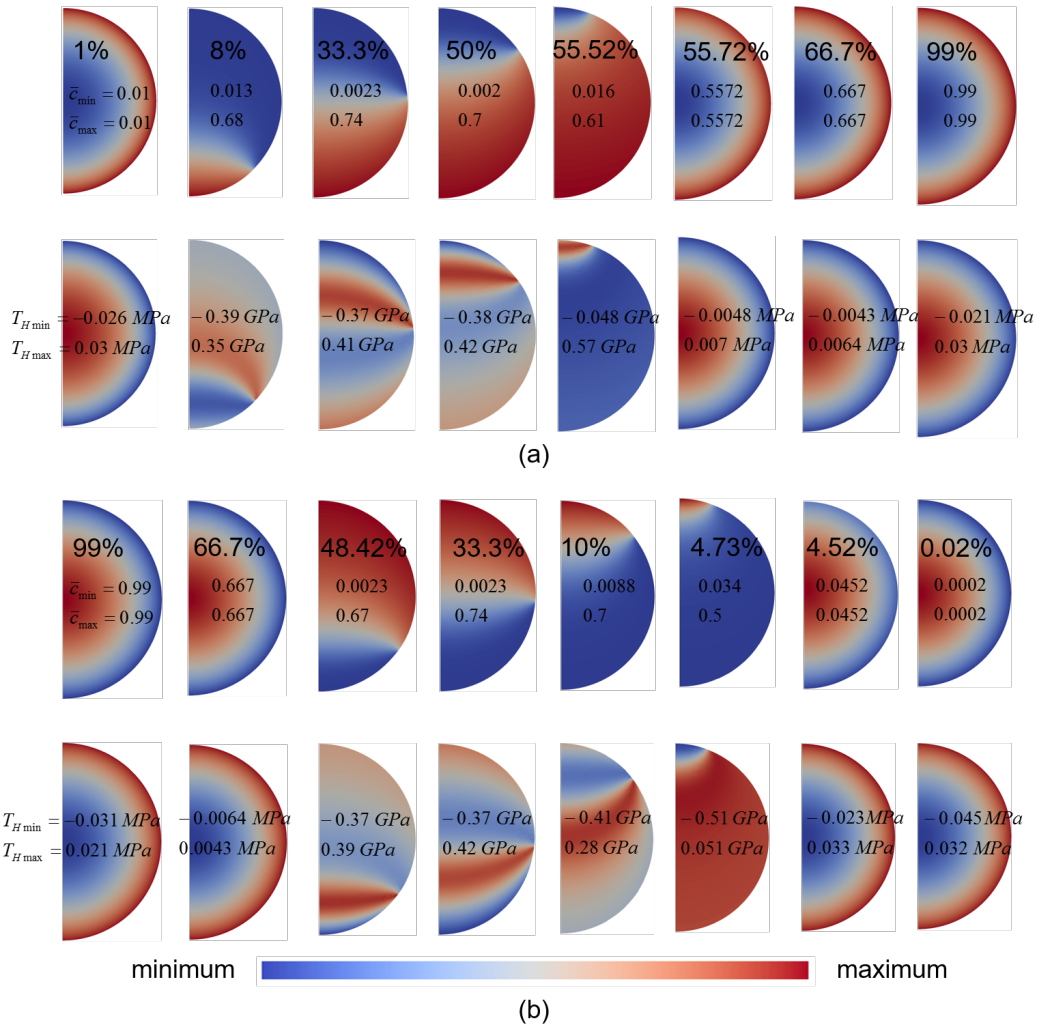

Fig. 4. Evolution of the microstructure and the corresponding hydrostatic stress as function of c_{avg}: (a) sodium insertion; (b) sodium extraction.

Next, we consider the sodium extraction process shown in Fig. 4b. At the beginning of sodium extraction, the system is in a single-phase state, showing the solid-solution phase Na_xFePO_4. Once c_{avg} is reduced to around 48.42%, a sodium-poor island is initiated around the "south pole" region,

which corresponds to the rapid dropping process of the system free energy shown in Fig. 3a. Here, c_{avg} required to initiate a phase separation matches the experimental observation in [8]. Similar to the insertion case, the system also exhibits the dynamics of single wave propagation with the same moving direction of the interface. Both, the phase behavior and the corresponding stress state are just reversed compared to the insertion process. The interface evolution is still the same as the insertion case, which is independent of the loading history. Indeed, the interface morphology is mainly controlled by the minimization of the system free energy. Thus, the two loading cases during phase changes share the same system free energy that is as low as possible, as shown in Fig. 3a. Such symmetrical phase behavior between insertion and extraction is consistent with the experimental observations [11], which indicates that a reversible state can be reached for NaFPO. When c_{avg} decreases to 4.73%, the sodium-poor phase will occupy all of the particle. It should be noticed that, different from sodium extraction, three phases ($FePO_4$, $Na_{2/3}FePO_4$, and $NaFePO_4$) can appear simultaneously at the nonequilibrium states during insertion, according to the experimental reports [4, 7, 10]. Casas-Cabanas et al. [4] pointed out that $NaFePO_4$ would be kinetically favored with respect to $Na_{2/3}FePO_4$ during insertion, but the equilibrium state would still be a two-phase segregation between $FePO_4$ and $Na_{2/3}FePO_4$ due to the fact that $NaFePO_4$ relaxes to $Na_{2/3}FePO_4$.

3.2. Role of the intermediate phase

To investigate the role of the intermediate phase, a control simulation is performed during insertion, in which, similar to LiFPO, the transformation from a sodium poor-phase $FePO_4$ into a sodium-rich phase $NaFePO_4$

occurs directly. Figs. 5a and 5b represent, at the center of the combined nucleation and spinodal zone of the range of phase segregated c_{avg}-states, the concentration as well as the corresponding hydrostatic stress plotted along the rotational axis AB for the control simulation and NaFPO. For comparison purposes, the relevant plots of LiFPO are also entered. As shown in Fig. 5a, although the solubility limits are the same, the interface from the control simulation is more diffuse than that of LiFPO. This is attributed to the reason that, the larger expansion of NaFPO, which is related to a larger cation radius of sodium, leads to the stronger suppressing effect of the coupling energy compared to LiFPO. We can analytically demonstrate that the system is totally stress-free provided that the species concentration depends linearly on the z-coordinate only, see Supplementary data for a detailed derivation. It means that the more diffuse the phase boundary is, the more minimized the stresses are. Thus, as shown in Fig. 5b, due to the relatively widened interface of the control simulation, the stress magnitudes in the interface region are smaller than those of LiFPO. However, in the absence of an intermediate phase in the control simulation, the stress levels at the two "pole" regions are larger compared to LiFPO. On the other hand, the formation of an intermediate phase induces an even more widened interface, leading to the lower cost of the interfacial energy penalty. Indeed, the interface between phases in NaFPO is more diffuse than that in LiFPO imaged by scanning transmission X-ray microscopy measurements [63]. As a result, in the presence of an intermediate phase, the stress magnitudes along the whole axis AB in a NaFPO particle are smaller than those from the case without an intermediate phase, and also much smaller compared to LiFPO.

Actually, this smoothed phase segregation of NaFPO shown in Fig. 5a can be experimentally verified by the work of Gaubicher et al. [8]. They pointed out that this striking smoothed phase segregation leads to a significant decrease in the lattice volume mismatch between the two phases, which could well compensate for known adverse effects such as the strain associated with the larger cation radius of sodium and the less efficient NIBs with respect to the solid electrolyte interphase in comparison to LIBs. Here, the formation of an intermediate phase for NaFPO can be justified by invoking an energy argument. We find that, in the absence of an intermediate phase, the total system free energy at the center of the combined nucleation and spinodal zone is almost 2.8 times larger than that of the structure with an intermediate phase. In this sense, the experimental observed intermediate state at $Na_{2/3}FePO_4$ [4–8, 10, 11] is energetically favorable. This is consistent with the result from density functional theory calculations that the intermediate phase $Na_{2/3}FePO_4$ is stable [64, 65]. As for LiFPO, both the experimental study [66] and density functional theory calculation [64] reveal that $Li_{2/3}FePO_4$ is metastable.

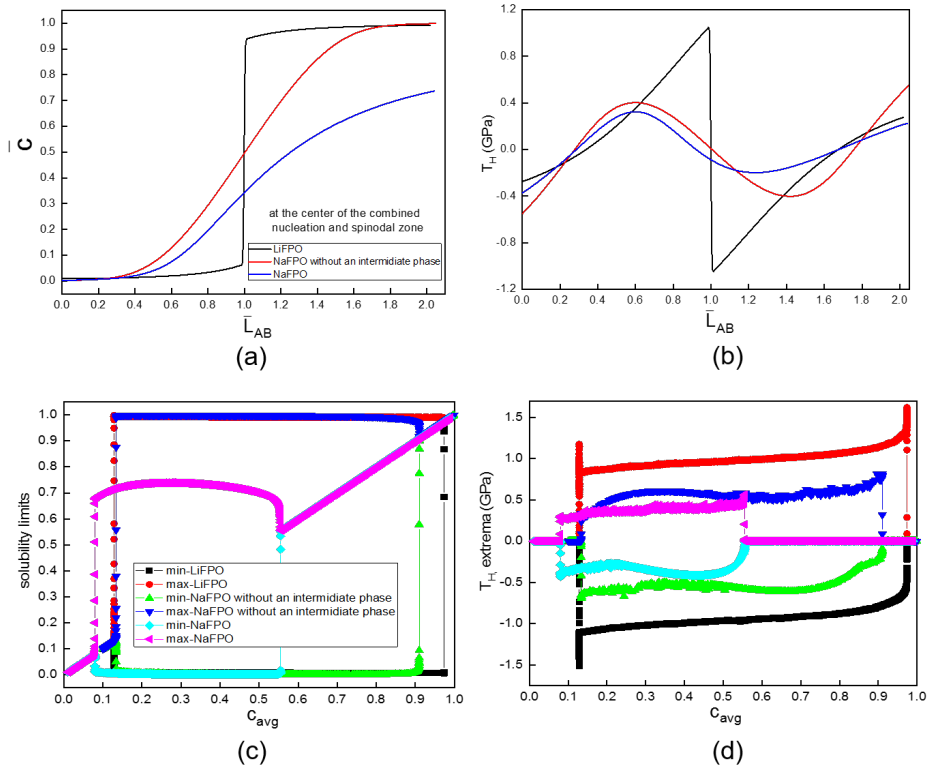

Fig. 5. Comparison of concentration and stresses from LiFPO, NaFPO without an intermediate phase, and NaFPO during insertion. (a) Normalized concentration and (b) normalized hydrostatic stress at the center of the combined nucleation and spinodal zone plotted along the rotational axis AB. (c) Solubility limits and (d) extrema of the hydrostatic stress as function of c_{avg}.

The above study is focused on the rotational axis AB at the center of the combined nucleation and spinodal zone. Now we extend it into the whole particle during the full insertion process in terms of the solubility limits and the extrema of the hydrostatic stress, as shown in Figs. 5c and 5d. Interestingly, in contrast to the fixed solubility limits found in the control simulation,

the formation of an intermediate phase leads to the varying solubility limits during phase changes, which is in excellent agreement with a recent in situ XRD study of NaFPO with the particle size of around 800 nm [7]. As will be discussed now, this can be attributed to the average concentration dependence of the stress assisted diffusion. If mechanics is not taken into account, NaFPO exhibits fixed solubility limits, see Fig. 3b. When mechanics is involved, the hydrostatic stress aids sodium transport towards the "south pole" region in the sodium-rich phase, and, at the same time, increases diffusion away from the "north pole" region in the sodium-poor phase. As illustrated in Fig. 4a, the stress gradient in each phase changes with the average concentration, meaning that the stress-driven diffusion correspondingly changes. As a result, the maximum solubility limit grows up to 0.74 when c_{avg} reaches 33.3% but shrinks afterwards, which results from the fact that the stress gradient in the sodium-rich phase gets gradually weakened after its peak. However, the minimum solubility limit slightly decreases during phase changes, owing to the gradually enhanced stress gradient in the sodium-poor phase. It should be noticed that the minimum solubility limit takes a value of 0.016 before the end of phase segregation, as shown in the fifth column of Fig. 4a. This is attributed to that the interface is close to the "north pole" region, leading to a tiny sodium-poor phase domain size. Therefore, NaFPO exhibits a dynamic solubility limits behavior during phase changes even for microsized particles. Actually, dynamic miscibility gap behavior is usually found in smaller nanoparticles, which may be related to the gradient energy evolution [17]. On the other hand, Fig. 5d demonstrates the reduction of the stresses induced by the intermediate phase. In the presence of an inter-

mediate phase, both the minima and maxima of the stresses in the whole particle of NaFPO are not only smaller than those from the case without an intermediate phase but also much smaller than those in a LiFPO particle for the whole phase-segregated states. Indeed, the overall stress levels in a NaFPO particle are over 2 times smaller than those in a LiFPO particle, although the volume expansion of NaFPO is much larger. This may seem counterintuitive at first glance due to the fact that a larger volume expansion of NaFPO leads to smaller stress states compared to LiFPO. For phase separating cathode materials, the stresses in active particles are induced by the lattice volume mismatch between the two phases at phase-segregated states. As mentioned before, both our work and the experimental study [8] reveal that this smoothed phase segregation of NaFPO leads to a significant decrease in the lattice volume mismatch between the two phases during phase changes. Thus, as a result of the competition between the different contributions towards minimizing the system free energy, including the elastic strain energy, the stresses in a NaFPO particle are lower, although the volume expansion of $FePO_4$ upon fully sodiation is larger than its lithium counterpart. Even more, no matter how large the volumetric strain is, a stress free strain state in the presence of volumetric strain due to intercalation can be reached if $\boldsymbol{\varepsilon} = \frac{1}{3}\Omega\left(c - c_0\right)\mathbf{I}$ is satisfied, meaning that the absense of any elastic strains. In this way, we have analytically demonstrated that an exactly z-linear concentration profile leads to stress-free strain states in Supplementary data. As a result, the formation of an intermediate phase not only accommodates the large volume change of about 17% but also induces a stress reduction behavior. Our new model of NaFPO theoretically verifies the

high strain-accommodation mechanism proposed by Casas-Cabanas et al. [4] that the formation of an intermediate phase acts as a buffer between $FePO_4$ and $NaFePO_4$ providing compliance to the structure. It should be noticed that, based on the shrinking-core concept of phase segregation, the 1D mechanically coupled simulation [30] shows that phase segregation of NaFPO is completely suppressed while it still occurs for LiFPO. This means that, in the presence of mechanics, the classical "core-shell" structure is extremely energetically unfavorable for NaFPO compared to LiFPO. In addition, Fig. 5d also shows that the maximum stress magnitude in a NaFPO particle is reached at the end of phase segregation just before the system enters the single-phase region, which is tensile and close to the interface region in the low concentration phase, see the fifth column of Fig. 4a.

3.3. Influence of the particle geometry

What is the influence of the particle geometry on the evolution of microstructure and stresses? We here study ellipsoidal particles which are symmetric under rotation around the z-axis. Two ellipsoidal particles are introduced: a prolate particle with the semi-axes $1/\sqrt{3}R_0$, $1/\sqrt{3}R_0$, $3R_0$; and an oblate particle with the semi-axes $\sqrt{3}R_0$, $\sqrt{3}R_0$, $1/3R_0$. Both of them share the same volume and boundary conditions as the spherical particle with the radius R_0. Fig. 6 shows the system free energy evolution of NaFPO during insertion by the solid lines for the two ellipsoidal particles, and the evolution of the microstructure and the corresponding hydrostatic stress are shown in Fig. 7. For comparison purposes, the plot of the system free energy evolution for the spherical particle is also entered in Fig. 6.

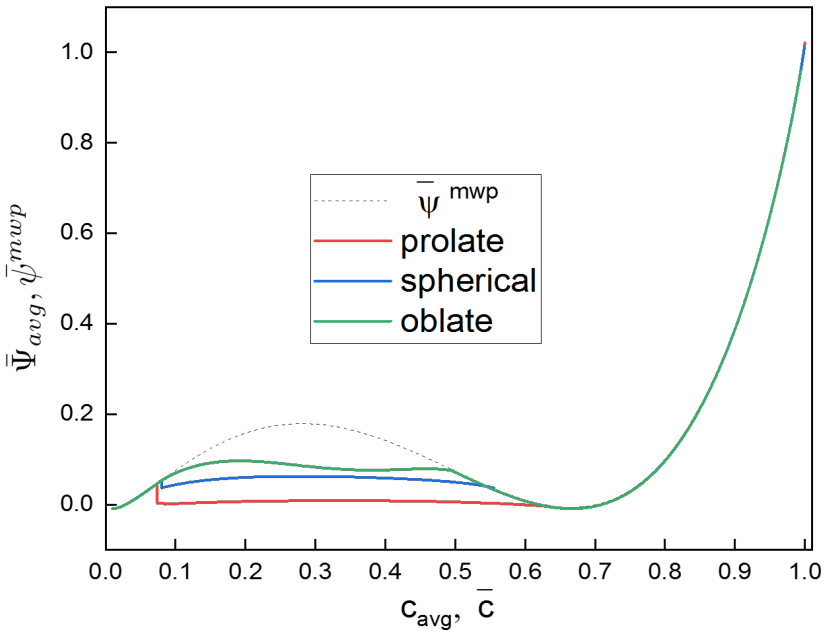

Fig. 6. Normalized average system free energy $\bar{\Psi}_{avg}$ and normalized multiwell potential $\bar{\psi}^{mwp}$ as function of c_{avg} and $\bar{c}$, respectively, for different particle geometry during insertion.

First, we focus on a prolate particle. In Fig. 7a, due to the prolate geometry, there is more surface per unit of particle volume in the vicinity of the "pole" region that possesses the maximum curvature, compared to the "equator" region. Thus, there is an enhanced sodium accumulation around the "pole" region, as shown in the first column of Fig. 7a. This is consistent with the reports for LIBs [41, 67–69]. As a result, phase segregation is initiated around the "south pole" region, which happens a little bit earlier than 8% for the spherical particle, and subsequently, a high concentration region

occurs also at the "north pole" region, see the second and third columns of Fig. 7a. Such phase segregation around a "pole" region enforces the formation of the phase boundary almost perpendicular to the z-axis such that the area of the phase boundary in a prolate particle is as small as possible. When c_{avg} approaches 8.453%, the sodium-rich island at the "north pole" region vanishes and the system enters a single wave propagation process, see the fifth column of Fig. 7a. Similar to the spherical particle, the phase boundary during quasi-equilibrium states is of a cap-like shape almost perpendicular to the rotational axis. During phase changes, most parts in each phase of the prolate particle are almost stress-free and stresses are mainly concentrated around the interface region. This means that the elastic strain energy in a prolate particle is low, which is in agreement with the simulation result from a 3D anisotropic phase-field model of LiFPO [49]. Therefore, compared to the spherical particle, the low elastic strain energy associated with a thin interface region leads to the lower system free energy in a prolate particle as can be seen in Fig. 6. When c_{avg} grows up to 63.61%, the prolate system enters the single-phase region, which is postponed compared to the spherical particle.

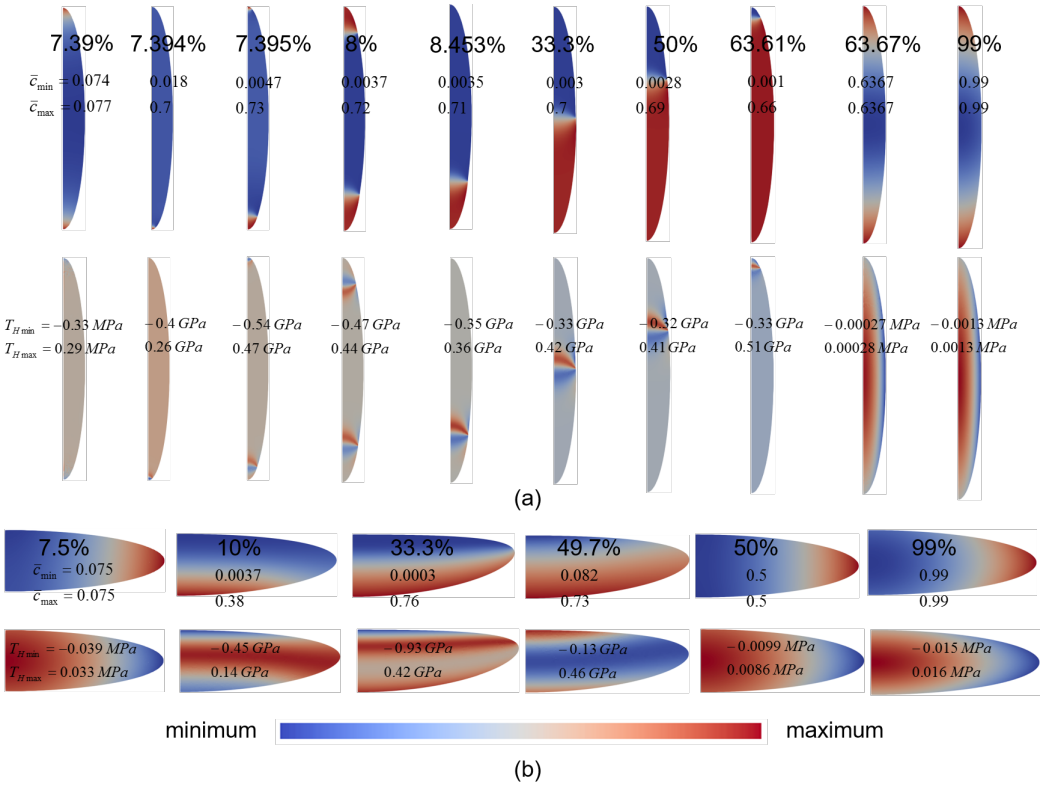

Fig. 7. Evolution of the microstructure and the corresponding hydrostatic stress as function of c_{avg} during insertion: (a) the prolate particle; (b) the oblate particle.

For an oblate particle as shown in Fig. 7b, interestingly, phase segregation is not initiated in the vicinity of the "equator" region that possesses the maximum curvature but around the "south pole" region and the phase boundary is almost perpendicular to the z-axis, leading to a relatively large interface region, see the second column of Fig. 7b. What is the reason behind that? According to the analytical solution of a stress-free z-linear concentration profile in Supplementary data, the phase-segregated states minimizing the elastic strain energy are those for which the phase boundary is extremely

diffuse and perpendicular to the rotational axis without ρ-dependence for the sodium concentration. As a result, the sodium-rich island in an oblate particle still occurs at the 'pole" region such that the concentration can be closer to a stress-free z-linear profile, meaning a lower contribution by the elastic strain energy to the system free energy, although the proportion of phase boundary is relatively large. c_{avg} required to initiate a phase separation increases up to around 10% compared to the spherical particle, since there is less surface per unit of particle volume in the vicinity of the "pole" region. To further elucidate the role of the elastic strain energy, a pure diffusion simulation is performed in an oblate particle. It is found that, in the absence of mechanics, the interface morphology is a cylindrical surface parallel to the rotational axis, and the area of the interface surface is smaller than that of the mechanically coupled diffusion case (we do not show this result here). Therefore, the interface morphology is dominated by the minimization of the elastic strain energy rather than the gradient energy. In contrast to the oblate particle, both the elastic strain energy and the gradient energy can be minimized by the same pattern in equilibrium states for the spherical and prolate particles. What is more, the overall stress levels in an oblate particle are larger compared to the spherical particle. As a result, the large stresses associated with a thick interface region induces the largest system free energy in an oblate particle among the three particles, as shown in Fig. 6. On the other hand, the single wave propagation process is terminated prior to c_{avg} of 50%, which indicates that the oblate particle has a broader single-phase region compared to the other two particles.

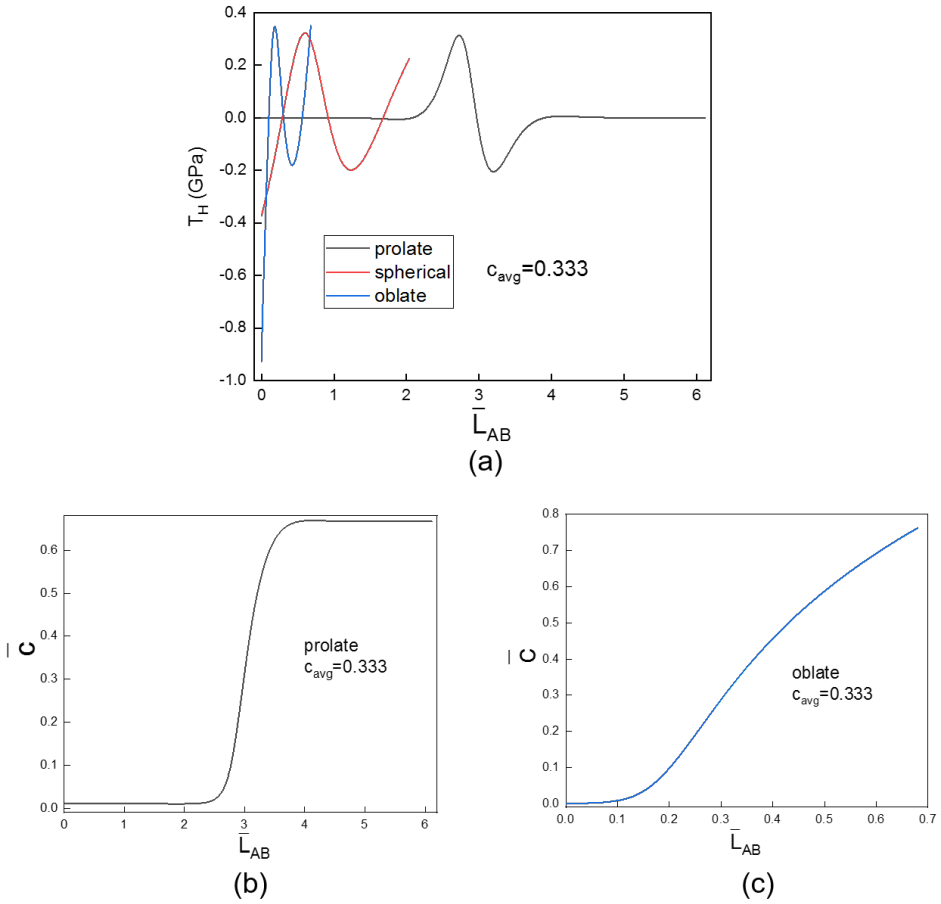

Fig. 8. (a) Normalized hydrostatic stress at $c_{avg} = 0.333$ plotted along the rotational axis AB for the different particle geometries during insertion. Normalized concentration at $c_{avg} = 0.333$ plotted along the rotational axis AB for (b) the prolate particle and (c) the oblate particle during insertion.

Now we compare the hydrostatic stress and the concentration at $c_{avg} = 0.333$ plotted along the rotational axis AB for the different particle geometries, as shown in Fig. 8. As described before, the prolate particle is nearly

stress-free in each phase, especially in the regions close to the tips, see Fig. 8a. This is due to the reason that the volume mismatch between two phases induces large stresses around the interface region, and the farther a material point is away from the interface, the less constrained it becomes. As a result, the prolate particle exhibits a nearly constant concentration in each phase, see Fig. 8b. However, in order to minimize the elastic strain energy in an oblate particle, the interface moves along a very short semi-axis of length $1/3R_0$, thus a steep stress gradient in each phase is evoked, which is more steep compared to the spherical particle. As a result, the oblate particle shows a strong inhomogeneity of the concentration in each phase, see Fig. 8c. Indeed, as discussed before, such a nearly linear concentration profile in an oblate particle minimizes the stresses and, thus, the elastic strain energy. On the other hand, as shown in Fig. 8a, both, the tensile stress magnitudes in the "south pole" region and the compressive stress magnitudes in the "north pole" region of the oblate particle are larger than those in a spherical particle. Especially in the "north pole" region, the compressive stress magnitudes are even over 2 times larger than those in a spherical particle. As a consequence, due to nearly stress-free phases, prolate particles are mechanically more reliable, and, thus, recommended for NIB electrode applications in view of mechanical stability and consequently better battery performance. On the other hand, the higher overall stress levels in oblate particles indicate that such kinds of particles are more prone to particle fracture and mechanical degradation, thus oblate particle shapes are not advised for NIB electrode applications. The above suggestions are in agreement with the results obtained by the 3D dilute solution model without phase segregation for the

cathode material $Li_xMn_2O_4$ of LIBs [67].

4. Conclusions

We have developed a chemo-mechanical phase-field model for NaFPO of NIBs which, as the major novelty, includes both, the two-phase segregation between $FePO_4$ and $Na_{2/3}FePO_4$, as well as the solid-solution phase Na_xFePO_4 $(2/3 < x < 1)$. In this way, the model accounts for the complex thermodynamics of phase segregation due to the existence of an intermediate phase and the elastic strain energy caused by the volume mismatch between phases. Based on this model, the microstructure evolution during the whole processes of insertion and extraction can be investigated for NaFPO. More general, the model can provide a significant input for the future phase-field work for NaFPO.

The stress assisted diffusion in the sodium-rich phase induces the striking behavior that the maximum solubility limit goes beyond 2/3 even in the two-phase region. The dynamics of single wave propagation occurs during sodium insertion/extraction. Since the system free energy follows the same path during insertion and extraction, this is taken as an indication of reversible behavior. We find that it is energetically favorable to form an intermediate phase for this material. In the presence of an intermediate phase, due to the average concentration dependence of the stress assisted diffusion, NaFPO exhibits varying solubility limits even for microsized particles, which matches recent experimental observation. The formation of an intermediate phase not only accommodates the large volume change of NaFPO but also

induces a stress reduction behavior by forming a more widened interface, as a consequence of which the overall stress level is over 2 times smaller than in a LiFPO particle.

In addition, the stresses can be minimized through optimization of the shape of NaFPO particles. Regardless of particle shape, the phase-segregated states minimizing the elastic strain energy are those for which the phase boundary is perpendicular to the rotational axis. This statement is supported by an analytical solution of a stress-free z-linear concentration profile. It is suggested that prolate particles are mechanically more reliable owing to nearly stress-free phases and thus suitable for NIB electrode applications, while oblate particles are more prone to mechanical degradation as a result of the higher overall stress levels.

The low-stress behavior due to the presence of an interemdiate phase can make NaFPO a promising cathode material for NIBs in the near future. Beyond our findings, we envision that the stress reduction behavior induced by an intermediate phase as found for NaFPO may hold in general and, thus, provides a new concept for improving the mechanical stability of phase separating electrode materials. Besides that, Lim et al. [70] suggest that an intermediate phase encountered in the NIB cathode material $Na_7V_4(P_2O_7)_4PO_4$ can reduce reaction barriers and thus give a better cell kinetics. Therefore, it can be a helpful concept for better battery performance to have in phase separating electrode materials an intermediate phase, although it is not easy to tune materials that do not possess such an inherent property towards such a property. It may be achieved by decreasing the particle size [14–17] or increasing the current density [15, 50, 52–54], which can modify the "spinodal

decomposition zone" of the multiwell potential curve at room temperature.

It has to be mentioned that we focus on the quasi-equilibrium states of the system using an extremely low C-rate in this work. Ohmer et al. [63] applied scanning transmission X-ray microscopy with its high chemical and spatial resolution to follow in situ the electrochemical lithiation/delithiation within a LiFPO single crystal. They reported an interesting filamentary growth of the $FePO_4$ phase along [010] upon dynamic delithiation, and concluded that such growth pattern is dominated by elastic effects rather than being transport-controlled. The mechanically coupled anisotropic phase-field model of NaFPO going beyond the quasi-equilibrium states will be subject of future work.

Acknowledgments

This work contributes to the research performed at CELEST (Center for Electrochemical Energy Storage Ulm-Karlsruhe) and was funded by the German Research Foundation (DFG) under Project ID 390874152 (POLiS Cluster of Excellence). The authors acknowledge support by the state of Baden-Württemberg through bwHPC.

Appendix A. Supplementary data

References

[1] V. Palomares, P. Serras, I. Villaluenga, K. B. Hueso, J. Carretero-González, T. Rojo, Energy & Environmental Science 5 (3) (2012) 5884–5901.

[2] J. Kim, D.-H. Seo, H. Kim, I. Park, J.-K. Yoo, S.-K. Jung, Y.-U. Park, W. A. Goddard III, K. Kang, Energy & Environmental Science 8 (2) (2015) 540–545.

[3] P. Moreau, D. Guyomard, J. Gaubicher, F. Boucher, Chemistry of Materials 22 (14) (2010) 4126–4128.

[4] M. Casas-Cabanas, V. V. Roddatis, D. Saurel, P. Kubiak, J. Carretero-González, V. Palomares, P. Serras, T. Rojo, Journal of Materials Chemistry 22 (34) (2012) 17421–17423.

[5] J. Lu, S. C. Chung, S.-i. Nishimura, A. Yamada, Chemistry of Materials 25 (22) (2013) 4557–4565.

[6] Y. Zhu, Y. Xu, Y. Liu, C. Luo, C. Wang, Nanoscale 5 (2) (2013) 780–787.

[7] M. Galceran, D. Saurel, B. Acebedo, V. V. Roddatis, E. Martin, T. Rojo, M. Casas-Cabanas, Physical Chemistry Chemical Physics 16 (19) (2014) 8837–8842.

[8] J. Gaubicher, F. Boucher, P. Moreau, M. Cuisinier, P. Soudan, E. Elkaïm, D. Guyomard, Electrochemistry communications 38 (2014) 104–106.

[9] N. Yabuuchi, K. Kubota, M. Dahbi, S. Komaba, Chemical reviews 114 (23) (2014) 11636–11682.

[10] W. Tang, X. Song, Y. Du, C. Peng, M. Lin, S. Xi, B. Tian, J. Zheng,

Y. Wu, F. Pan, et al., Journal of Materials Chemistry A 4 (13) (2016) 4882–4892.

[11] K. Xiang, W. Xing, D. B. Ravnsbæk, L. Hong, M. Tang, Z. Li, K. M. Wiaderek, O. J. Borkiewicz, K. W. Chapman, P. J. Chupas, et al., Nano Letters 17 (3) (2017) 1696–1702.

[12] J. Dodd, R. Yazami, B. Fultz, Electrochemical and Solid-State Letters 9 (3) (2006) A151–A155.

[13] N. Shpigel, S. Sigalov, M. D. Levi, T. Mathis, L. Daikhin, A. Janes, E. Lust, Y. Gogotsi, D. Aurbach, Joule 2 (5) (2018) 988–1003.

[14] M. Wagemaker, D. P. Singh, W. J. Borghols, U. Lafont, L. Haverkate, V. K. Peterson, F. M. Mulder, Journal of the American Chemical Society 133 (26) (2011) 10222–10228.

[15] D. A. Cogswell, M. Z. Bazant, ACS Nano 6 (3) (2012) 2215–2225.

[16] M. J. Welland, D. Karpeyev, D. T. O'Connor, O. Heinonen, ACS Nano 9 (10) (2015) 9757–9771.

[17] T. Zhang, M. Kamlah, Electrochimica Acta 298 (2019) 31–42.

[18] M. Klinsmann, D. Rosato, M. Kamlah, R. M. McMeeking, Journal of power sources 331 (2016) 32–42.

[19] R. Xu, K. Zhao, Journal of the Mechanics and Physics of Solids 121 (2018) 258–280.

[20] D. Chen, D. Kramer, R. Mönig, Electrochimica Acta 259 (2018) 939–948.

[21] M. Klinsmann, D. Rosato, M. Kamlah, R. M. McMeeking, Journal of the Mechanics and Physics of Solids 92 (2016) 313–344.

[22] Z. Guo, T. Zhang, H. Hu, Y. Song, J. Zhang, Journal of Applied Mechanics 81 (3) (2014) 031013.

[23] C. V. Di Leo, E. Rejovitzky, L. Anand, Journal of the Mechanics and Physics of Solids 70 (2014) 1–29.

[24] T. Zhang, Z. Guo, Modelling and Simulation in Materials Science and Engineering 22 (2) (2014) 025016.

[25] C. V. Di Leo, E. Rejovitzky, L. Anand, International Journal of Solids and Structures 67 (2015) 283–296.

[26] M. Ganser, F. E. Hildebrand, M. Kamlah, R. M. McMeeking, Journal of the Mechanics and Physics of Solids 125 (2019) 681–713.

[27] Y. Zhao, P. Stein, Y. Bai, M. Al-Siraj, Y. Yang, B.-X. Xu, Journal of Power Sources 413 (2019) 259–283.

[28] T. Zhang, M. Kamlah, Continuum Mechanics and Thermodynamics (2018) 1–20.

[29] J. W. Cahn, J. E. Hilliard, The Journal of Chemical Physics 28 (2) (1958) 258–267.

[30] T. Zhang, M. Kamlah, Journal of The Electrochemical Society 165 (10) (2018) A1997–A2007.

[31] T. Zhang, M. Kamlah, Journal of The Electrochemical Society 167 (2) (2020) 020508.

[32] M. Huttin, M. Kamlah, Applied Physics Letters 101 (13) (2012) 133902.

[33] B. Han, A. Van der Ven, D. Morgan, G. Ceder, Electrochimica Acta 49 (26) (2004) 4691–4699.

[34] M. E. Gurtin, Physica D: Nonlinear Phenomena 92 (3-4) (1996) 178–192.

[35] N. G. Hörmann, A. Groß, Physical Review Materials 3 (5) (2019) 055401.

[36] N. Nadkarni, T. Zhou, D. Fraggedakis, T. Gao, M. Z. Bazant, Advanced Functional Materials (2019) 1902821.

[37] O. Redlich, A. Kister, Ind Eng Chem 24 (1948) 345–52.

[38] C. Birkl, E. McTurk, M. Roberts, P. Bruce, D. Howey, Journal of The Electrochemical Society 162 (12) (2015) A2271–A2280.

[39] M. Huttin, Phase-field modeling of the influence of mechanical stresses on charging and discharging processes in lithium ion batteries, Ph.D. thesis, Karlsruhe Institute of Technology, Karlsruhe (2014).

[40] Y. Zeng, M. Z. Bazant, SIAM Journal on Applied Mathematics 74 (4) (2014) 980–1004.

[41] Y. Zhao, P. Stein, B.-X. Xu, Computer Methods in Applied Mechanics and Engineering 297 (2015) 325–347.

[42] D. Morgan, A. Van der Ven, G. Ceder, Electrochemical and Solid State Letters 7 (2) (2003) A30.

[43] R. Malik, D. Burch, M. Bazant, G. Ceder, Nano Letters 10 (10) (2010) 4123–4127.

[44] R. Amin, P. Balaya, J. Maier, Electrochemical and Solid State Letters 10 (1) (2006) A13.

[45] L. Hong, L. Li, Y.-K. Chen-Wiegart, J. Wang, K. Xiang, L. Gan, W. Li, F. Meng, F. Wang, J. Wang, et al., Nature communications 8 (1) (2017) 1–13.

[46] M. Tang, J. F. Belak, M. R. Dorr, The Journal of Physical Chemistry C 115 (11) (2011) 4922–4926.

[47] K. Yang, M. Tang, Journal of Materials Chemistry A 8 (6) (2020) 3060–3070.

[48] G. K. Singh, G. Ceder, M. Z. Bazant, Electrochimica Acta 53 (26) (2008) 7599–7613.

[49] A. Van der Ven, K. Garikipati, S. Kim, M. Wagemaker, Journal of the Electrochemical Society 156 (11) (2009) A949–A957.

[50] P. Bai, D. A. Cogswell, M. Z. Bazant, Nano letters 11 (11) (2011) 4890–4896.

[51] D. A. Cogswell, M. Z. Bazant, Nano Letters 13 (7) (2013) 3036–3041.

[52] N. Sharma, X. Guo, G. Du, Z. Guo, J. Wang, Z. Wang, V. K. Peterson, Journal of the American Chemical Society 134 (18) (2012) 7867–7873.

[53] H. Liu, F. C. Strobridge, O. J. Borkiewicz, K. M. Wiaderek, K. W. Chapman, P. J. Chupas, C. P. Grey, Science 344 (6191).

[54] M. Hess, T. Sasaki, C. Villevieille, P. Novák, Nature communications 6 (1) (2015) 1–9.

[55] C. Delacourt, M. Safari, Electrochimica Acta 56 (14) (2011) 5222–5229.

[56] Y. Song, Z. Li, A. Soh, J. Zhang, Mechanics of Materials 91 (2015) 363–371.

[57] T. Maxisch, G. Ceder, Physical Review B 73 (17) (2006) 174112.

[58] D. Gaston, C. Newman, G. Hansen, D. Lebrun-Grandie, Nuclear Engineering and Design 239 (10) (2009) 1768–1778.

[59] G. Chen, X. Song, T. J. Richardson, Electrochemical and Solid-State Letters 9 (6) (2006) A295–A298.

[60] L. Laffont, C. Delacourt, P. Gibot, M. Y. Wu, P. Kooyman, C. Masquelier, J. M. Tarascon, Chemistry of Materials 18 (23) (2006) 5520–5529.

[61] C. Delmas, M. Maccario, L. Croguennec, F. Le Cras, F. Weill, Nature Materials 7 (8) (2008) 665–671.

[62] C. Ramana, A. Mauger, F. Gendron, C. Julien, K. Zaghib, Journal of Power Sources 187 (2) (2009) 555–564.

[63] N. Ohmer, B. Fenk, D. Samuelis, C.-C. Chen, J. Maier, M. Weigand, E. Goering, G. Schütz, Nature communications 6 (1) (2015) 1–7.

[64] F. Boucher, J. Gaubicher, M. Cuisinier, D. Guyomard, P. Moreau, Journal of the American Chemical Society 136 (25) (2014) 9144–9157.

[65] A. Saracibar, J. Carrasco, D. Saurel, M. Galceran, B. Acebedo, H. Anne, M. Lepoitevin, T. Rojo, M. C. Cabanas, Physical Chemistry Chemical Physics 18 (18) (2016) 13045–13051.

[66] Y. Orikasa, T. Maeda, Y. Koyama, H. Murayama, K. Fukuda, H. Tanida, H. Arai, E. Matsubara, Y. Uchimoto, Z. Ogumi, Journal of the American Chemical Society 135 (15) (2013) 5497–5500.

[67] P. Stein, B. Xu, Computer Methods in Applied Mechanics and Engineering 268 (2014) 225–244.

[68] Z. Guo, L. Ji, L. Chen, Journal of Materials Science 52 (23) (2017) 13606–13625.

[69] J. Santoki, D. Schneider, M. Selzer, F. Wang, M. Kamlah, B. Nestler, Modelling and Simulation in Materials Science and Engineering 26 (6) (2018) 065013.

[70] S. Y. Lim, H. Kim, J. Chung, J. H. Lee, B. G. Kim, J.-J. Choi, K. Y. Chung, W. Cho, S.-J. Kim, W. A. Goddard, et al., Proceedings of the National Academy of Sciences 111 (2) (2014) 599–604.